SHEAR-SELECTED CLUSTERS FROM THE DEEP LENS SURVEY

David Wittman
Bell Labs, Lucent Technologies
700 Mountain Avenue, Murray Hill, NJ 07974

Representing the DLS Collaboration

ABSTRACT

The Deep Lens Survey (DLS) is a deep multiwavelength imaging survey of 28 square degrees of sky, involving 100 nights of 4-meter telescope time. Our primary goal is to use weak gravitational lensing both to find specific mass concentrations (clusters) and to measure weak lensing by large-scale structures (cosmic shear). This paper focuses on clusters. Because lensing is sensitive to all types of matter, not only luminous matter, it allows us to compile a sample of clusters selected by mass. This is important because it is the cluster mass function which is an important diagnostic of cosmological parameters. All samples to date have been detected through their stellar light or X-ray emission, which may miss underluminous clusters and may not truly represent the mass function. A mass-selected sample will yield a less biased mass function and perhaps some intrinsically interesting "dark" clusters. We present a summary of the DLS, the techniques we use to find clusters, and a preliminary version of the DLS shear-selected cluster sample.

1 Introduction

1.1 Gravitational Lensing and Photometric Redshifts

The Deep Lens Survey (DLS) is an attempt to combine the two recently-developed techniques of weak gravitational lensing and photometric redshifts. The goal of this Introduction is to demonstrate to a wide audience why that combination is quite powerful. Readers familiar with these techniques may wish to skip to the next section, which examines the specifics of the DLS in some detail.

It has long been known that most of the matter in the universe is dark. This is a problem for astronomers who would like to make observations of structure in the universe. They have had to resort to some approximations and indirect evidence to arrive at measurements. For example, to measure the mass of a cluster of galaxies, the assumption is made that it is bound and virialized, so that one can derive a mass from the dispersion of individual galaxy velocities. If clusters are actually flying apart, all bets are off.

Approximations such as these have actually been surprisingly useful. Estimates of the mean matter density of the universe, Ω_m, derived this way are in broad agreement with results from WMAP,[1] for example. However, we would like to observe the large-scale distribution of dark matter more directly for several reasons. First, we would like to have late-time estimates of structure which are as accurate as possible, to provide some complementarity to the exquisite WMAP measurements of structure in the early universe. Second, direct observations would make for much easier comparisons with numerical simulations of structure formation, because the complexities of galaxy and star formation cannot yet be adequately simulated. Third, we know that the standard astrophysical approximations are not valid in some environments (for example, we know that some clusters are *not* in equilibrium), and we would rather not simply eliminate these environments from our structure measurements. Fourth, inferring the mass of luminous systems is not the same as detecting mass wherever it lies. It is possible if not likely that there are massive systems which are underluminous enough to have escaped detection with traditional methods.

The most direct way of detecting mass on large scales is through weak gravitational lensing. Light rays traveling to us from distant "background" sources are deflected by gravitational potentials they encounter on the way (Figure 1). They undergo a displacement and a magnification which we cannot easily measure, and a shear which we can

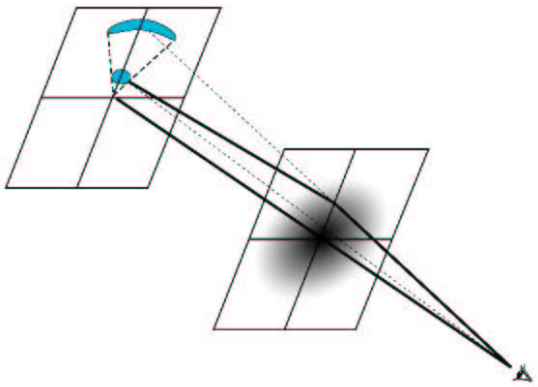

Fig. 1. Schematic view of gravitational lensing. At left, there is a source with an intrinsically circular shape. The intervening mass (center) bends the light rays which reach the observer (right), presenting the observer with an image which is displaced and stretched (left, top). Although the observer does not know the true shape of any source, weak lensing is revealed by shape correlations in a population of background galaxies.

measure statistically by assuming that in the absence of lensing, galaxy shapes are randomly aligned (this is not strictly true in all cases, but is a good approximation for the DLS). The shear is a function of the lens mass distribution and the (angular diameter) distances between observer, lens, and source. One measures only redshifts and angles, rather than emission from astrophysical processes in the cluster.

However, until recently, lensing work focused entirely on mass measurements of already-known clusters. A great deal of dark matter was found in such clusters, but there was little opportunity to explore any selection effects which might be present in the underlying cluster samples. The first suggestion that clusters could be *discovered* with weak lensing came in 1996 (Ref. 2). Driven by advances in detectors, this goal is finally being realized. The same advances in detectors allow us to measure *cosmic shear*, or weak lensing by large-scale structure. This measurement is more difficult than for clusters because the signal is much lower, but the benefit is that it provides information over a range of the power spectrum rather than just on the most massive overdensities.

So why do we need photometric redshifts? Because it is impractical to obtain spectroscopic redshifts for all the sources in weak lensing, no advantage has been taken of the dependence on distance ratios. Instead, papers on clusters generally assume that all sources are effectively at some mean distance ratio which is plausible given the depth of the imaging and the known spectroscopic redshift of the cluster. But if redshifts were

available for each source, the increase of shear with source redshift would allow us to locate structure along the line of sight. If claims of "dark" clusters prove to be true, this tomographic technique will be the *only way* to derive the redshifts of such lenses. Lens redshifts in turn are required to derive masses and mass-to-light ratios, so this is the only way of measuring how dark a dark lens is. Furthermore, a shear-vs-redshift test enhances the credibility of a dark cluster claim by splitting a single shear measurement into independent bins, each of which must follow the expected trend. Finally, separating sources by redshift should lead to higher signal-to-noise mass measurements of any target, because one is no longer averaging small shears (from sources immediately behind the lens) together with large ones (from very distant sources).

For cosmic shear, the source redshift issue is usually addressed by deducing some plausible distribution, which is then convolved with models of structure formation as a function of redshift to yield predictions for each model, to be compared with the observations. In other words, we obtain only a single measure of structure integrated along a very long line of sight. With redshifts, we could actually look at the development of structure with cosmic time. This would be a much more stringent test of models.

Spectroscopic redshifts are impossible for all these faint sources, so we derive photometric redshifts by imaging at several different wavelengths. These "colors" allow us to estimate the redshift of each source to some accuracy which depends on the number and wavelength range of the bandpasses. When combined with shear information, this extends the nice properties of weak lensing mass measurements—independence from star formation history, baryon content, and dynamics—into the third dimension. The DLS thus can measure structure as a function of cosmic time.

1.2 Shear-Selected Clusters*

If clusters are useful as cosmological probes, it is because they represent large overdensities, which evolve differently under different scenarios. For direct comparison with theory and with n-body simulations, therefore, we would like to detect clusters based on their mass. Historically, though, they have been detected based on emitted light from galaxies[3,4] or X-rays from a hot intracluster medium.[5] These measurements can be converted to mass estimates under certain assumptions, but even if that is done with perfect accuracy, underluminous clusters may well be missing from these samples. This

*Astronomers often use "baryonic matter" as a shorthand for "matter other than dark matter", including leptons. That meaning carries over to terms such as "baryon fraction" and the like.

is why a selected on the basis of weak lensing shear is so important.

Note that shear does not depend only on mass. It is also proportional to the distance ratio $\frac{D_{ls}D_l}{D_s}$ where D_l, D_{ls}, and D_s are the angular diameter distances from observer to lens, lens to source, and observer to source, respectively. Convolution of shear measurements yields an estimate of dimensionless surface mass density or convergence κ:

$$\kappa = \Sigma/\Sigma_{\rm crit}$$
$$\Sigma_{\rm crit} = \frac{D_{ls}D_l}{D_s}\frac{4\pi G}{c^2}$$

Interestingly, for reasonable lens and source redshifts, $\Sigma_{\rm crit} \sim 1$ gm cm^{-2}.

Thus for a given lens, more distant background sources are more highly sheared. If instead we fix the redshift of the background source and vary the lens redshift (keeping its mass fixed), the shear follows the function plotted in Figure 2. This, combined with the source redshift distribution of a survey, is the relevant quantity in determining the sensitivity of a survey to clusters as a function of mass and redshift. The lensing efficiency is a very broad function, making weak lensing surveys sensitive to a broad range of redshifts, as long as there are sufficient sources at $z \sim 1$ or higher. This redshift sensitivity is very different from optical and X-ray selection, which fall off as the square of the luminosty distance. Despite that, advances in instrumentation now enable optical and X-ray selection up to and beyond $z \sim 1$, so there is a great deal of overlap among the methods.

There is also an exciting new method based on the Sunyaev-Zel'dovich effect (SZE), or upscattering of CMB photons by the hot intracluster gas.[6] This method has an extremely deep redshift sensitivity, because its source is at $z \sim 1100$, and it avoids the luminosity issue entirely because it is based on scattering of the background. SZE samples are on the way, and it will be extremely informative to compare samples produced by the four different methods. However, the SZE tells us only about baryons in the cluster. A total mass would have to be inferred from an assumed baryon fraction, or from the combination of SZE with other data. Thus lensing will continue to play a vital role.

Surveying for clusters via shear selection is still in its infancy. There are only two shear-selected masses with confirmed spectroscopic redshifts.[7,8] Several other groups have identified several shear-selected masses with redshifts roughly determined from two-color photometry.[9,10] Together these four examples span the redshift range 0.27—0.68.

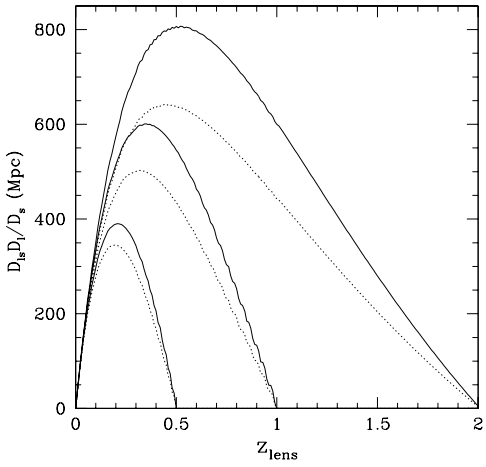

Fig. 2. Shear as a function of lens redshift, for several values of source redshift (which correspond to the right-hand end of each curve). The two curves for each source redshift demonstrate the effect of changing the cosmology, which is nearly degenerate with changing the lens mass. The lensing efficiency is a very broad function, making weak lensing surveys sensitive to a broad range of redshifts.

In other cases,[11–14] the object causing the shear is not clearly identifiable and in some cases has been called a "dark cluster". Weinberg & Kamionkowski[15] calculate that up to 20% of clusters in shear-selected surveys are expected to be optically dark. However, without a redshift, the masses of these "dark clusters" cannot be computed. Hence mass-to-light ratios (or even limits) cannot be computed either, and it is unclear just how dark these clusters are. Nonspectroscopic means of determining their redshifts (and therefore masses and derived parameters) must be developed.

2 The Deep Lens Survey

2.1 Basic Parameters of the DLS

Instrument: We chose the Kitt Peak National Observatory (KPNO) and Cerro Tololo Inter-American Observatory (CTIO) 4-m telescopes for their good combination of aperture and field of view. Each telescope is equipped with an 8k $\times$ 8k Mosaic imager (Muller *et al.* 1998), providing a $35'$ field of view with $0.25''$ pixels and very small gaps between three-edge-buttable devices. A further strength is that with some observing

with each of two similar setups, we can provide a check on systematic errors due to optical distortions, seeing, and the like, without sacrificing homegeneity of the dataset in terms of depth, sampling, and so on.

Filter set: We set our goal for photometric redshift accuracy at 20% in $1+z$. This is quite modest in comparison to the state of the art, but we do not need better accuracy. A bigger contribution to the error on a lensing measurement from any one galaxy is shape noise, the noise stemming from the random unlensed orientations of galaxies. Thus we do not need great redshift accuracy on each galaxy, but we do need the redshifts to be unbiased in the mean. This accuracy can be achieved with only four filters in the 0.3–1 μm wavelength range in which CCDs perform well. We chose the Johnson-Cousins B, V, and R filters and the Sloan Digital Sky Survey (SDSS) z' filter. The z' filter was chosen because it goes to somewhat longer wavelength and is therefore sensitive to a given spectral feature at somewhat higher redshift. Given that the main spectral feature of most galaxies is at 0.4 μm, our filter set is expected to yield reasonable photometric redshifts up to $z \sim 1.5$. Although higher redshifts would be desirable, covering large areas of sky deeply with current ground-based infrared arrays is impractical. We did not adopt the entire SDSS filter set because, at the blue end, u' would incur significant losses from the prime focus correctors. We therefore chose B as our bluest filter, and filled in the range between B and z' with the wide V and R filters.

Depth: Our depth goal is a 1-σ sky noise of 29 mag arcsec^{-2} in BVR and 28 in z', which required total exposure times of 12 ksec in BVz' and 18 ksec in R, for a total of 54 ksec exposure on each patch of sky (see below for discussion). We divided this total time into 20 exposures of 600 (900) seconds each in BVz' (R). Twenty exposures was a compromise between efficiency (given a read time of ~ 140 seconds) and the need to take many dithered exposures to obtain good dark-sky flats.

Area: In order to study the mass clustering on linear scales (out to $15h^{-1}$ Mpc at z=0.3), we must image $2^\circ \times 2^\circ$ regions of the sky. With Mosaic providing a $40'$ field of view after dithering, we assemble each 2° field from a 3×3 array of Mosaic-size subfields. Thus each field requires a total exposure time of 9×54 ksec, or 486 ksec. The number of such fields should be as large as possible to get a handle on cosmic variance. To fit the entire program into a reasonable amount of telescope time, we decided on five fields. Thus the total exposure time for the survey is 2.43 Msec. Field locations were selected without regard to the presence of already-known structures, making the survey unbiased with respect to cluster mass and redshift distributions. Practical aspects of field selection, such as overlap with complementary survey, is described elsewhere.[16]

Resolution: In ground-based optical astronomy, resolution is limited by atmospheric turbulence, also called "seeing." Subarcsecond resolution is common for individual exposures on these telescopes, but achieving this resolution in the final product of a large survey is another matter, as a large range of seeing conditions is to be expected. We address this problem by observing in R when the seeing conditions are $0.9''$ or better, and switching to B, V, or z' when the seeing becomes worse than $0.9''$. Thus the final R images are guaranteed to be $0.9''$ or better. We then make the weak lensing shape measurements in R and use the other filters only for color information.

Time: The number of nights is then determined by the observing efficiency. The maximum possible efficiency given the ratio of our exposure times and the read time of the Mosaic is 82%, but in practice the efficiency is 70% due to instrument and telescope failures. Thus about 3.5 Msec or 1000 hours of dark time is required, or 100 10-hour cloudless nights.

2.2 The DLS in Context

This is a golden age for optical surveys of the sky, as it has finally become practical to fill the entire focal plane of a large, wide-field telescope with sensitive, linear CCD imagers. Because this conference is aimed at a broad audience, it is worth taking a moment to highlight the differences between the DLS and the other currently ongoing optical surveys contributing to these proceedings, the SDSS.

The SDSS is covered in detail elsewhere in these proceedings,[17] but a brief description for context is in order. The SDSS covers ~ 5000 deg^2 to a "depth" of ~ 5 galaxies arcmin^{-2}. (Depth is usually quoted in terms of a magnitude limit for some type of detection, but the number of sources per square arcminute is probably more meaningful to a wide audience.) The SDSS is wonderfully suited to tracing the galaxy distribution to $z \sim 0.3$, the cluster distribution to $z \sim 0.5$, and the quasar distribution to very high redshifts.

The DLS covers 200 times less area, but goes 10 times "deeper," ~ 50 galaxies arcmin^{-2}. This makes it better suited for detailed studies of individual clusters, particularly lensing studies which require images of many galaxies *behind* the cluster. Furthermore, the DLS is better suited for lensing because it has better angular resolution ($\sim 0.9''$ in R *vs.* $\sim 1.5''$ for the SDSS). Of course, the SDSS has made an impact on weak lensing. Because of its massive statistics, it is well suited to determining average mass profiles of different types of galaxies by "stacking" the lensing signal around a

sample of foreground galaxies of a given type.[18] This procedure is called galaxy-galaxy lensing; the stacking is necessary because the signal from one foreground galaxy is far too weak to detect. The SDSS has also determined the average profile of clusters by "stacking" the signal from a sample of clusters,[19] but it is not well suited to measuring the profile of an individual cluster.

The DLS is suited to measuring individual cluster profiles, because it detects so many more sources in the background of each cluster. For the same reason, it allows *searches* for new clusters via weak lensing. It also better suited for studying the redshift evolution of various properties, because it reaches further in redshift. For example, changes in the average galaxy mass profile with cosmic time may be measurable by the DLS. More importantly, changes in the cluster abundance and mass function will be detectable. The changes in these quantities from $z \sim 0$ to $z \sim 1$ depend rather sensitively on cosmological parameters such as Ω_m, the matter density of the universe, and σ_8, the rms fluctuations on $8h^{-1}$ Mpc scales. Thus the DLS is designed to be deep enough to detect and measure the mass of clusters at $z \sim 1$.

There are *many* other important optical surveys: NOAO Wide-Deep,[20] VIRMOS,[21] Subaru,[22] CFH Legacy[23] to name a few, and each has its strengths. We do not mean to slight them by not discussing them here. By focusing on SDSS and DLS, we have attempted to highlight the different roles of wide and of deep surveys.

2.3 The DLS in Operation

We take roughly 5 GB of deep exposures in each good night at the telescope, plus roughly an equal amount of calibration data. Runs are typically 4-6 nights with 4-5 runs per year. Data are written to tape at the observatory and brought back to Bell Labs and Brown University for calibration and analysis. Roughly 80% of the planned data have been taken, and spring 2004 will mark the completion of data acquisition barring losses due to weather.

The basic steps for reducing a run are:

- Removal of instrumental signatures such as sensitivity variations.
- Astrometric calibration.
- Photometric calibration.

These steps follow standard procedures and are described more fully elsewhere.[16] Data from multiple runs are then combined and analyzed in these steps:

- For R-band images, characterization and treatment of the point-spread function (PSF).
- Coaddition of multiple images covering the same area of sky in a single filter (stacking).
- Characterization and treatment of the PSF of the stacked image (R only).
- Detection and cataloging of sources on a single deep image.
- Measuring the shapes of cataloged galaxies more precisely (R only).
- Matching the B, V, R, and z' catalogs corresponding to a given area of sky (optional).
- Cleaning the catalog of spurious detections.
- Computing photometric redshifts (optional).
- Weak lensing analysis of the shape (and optionally redshift) statistics.

Several steps are labeled optional here because they cannot be completed until an area has been surveyed in all four filters. To conduct a preliminary analysis before all the data have been taken, we have analyzed the R-band catalog alone in a traditional lensing analysis which yields a two-dimensional map of mass projected along the line of sight. This map is sufficient to identify mass concentrations, which will then be followed up with the more sophisticated three-dimensional analysis when all the data are in.

We do not describe most of these steps in detail here, but we do wish to highlight the most lensing-specific step, the treatment of the PSF. The final step, weak lensing analysis of the shape and redshift statistics, will be detailed in the next section.

The first step is necessary because anisotropies in the PSF could mimic a lensing signal. The left panel of Figure 3 illustrates the problem by encoding as sticks the position angle and ellipticity of point sources (stars) in one exposure of one of the eight Mosaic CCDs. PSFs on most telescopes tend to be $\sim 1-10\%$ elliptical due to focus and guiding errors. This is much larger than the lensing signal we are looking for, but difficult to control at the telescope due to changing temperatures and wind and gravity loads on the optics. Thus we make the PSF as isotropic as possible in post-processing. This is done by convolving the image with a kernel with ellipticity components opposite to that of the PSF (Fischer & Tyson 1997). Because the PSF shape is position-dependent, the kernel must be also. The result is shown in the right panel of Figure 3. The PSF shapes are much closer to round, and the remaining ellipticities are not spatially correlated as a lensing signal would be.

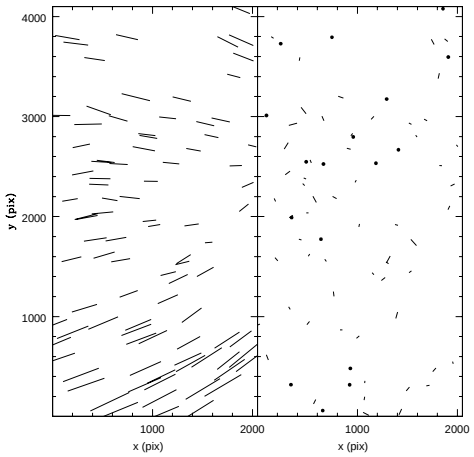

Fig. 3. Point-spread function correction in one 2k×4k CCD. Shapes of stars, which as point sources should be perfectly round, are represented as sticks encoding ellipticity and position angle. Left panel: raw data with spatially varying PSF ellipticities up to 10%. Right panel: after convolution with a spatially varying asymmetric kernel, ellipticities are vastly reduced (stars with $\epsilon < 0.5\%$ are shown as dots), and the residuals are not spatially correlated as a lensing signal would be.

This correction is necessary for each exposure because observing conditions change from exposure to exposure. Even within an exposure, the procedure is applied separately for each CCD, in case there are piston differences between the CCDs. Each CCD typically has 50–100 unsaturated, unambiguous stars, which provide for a second-order polynomial fit to the spatial variation. We also apply this procedure to the combined R image, to reduce the effects of any small registration errors. In this case, we find ~ 1000 stars and use a fourth-order polynomial fit.

3 The DLS Shear-Selected Cluster Sample

3.1 Construction of the Sample

The DLS is taking data over a five-year period, but a first cluster sample can be constructed before all the data are in. This is because massive clusters can be detected even in not-so-deep imaging, and because a large contiguous area is not required for an unbiased sample of clusters. We chose all subfields for which we had at least 9000 seconds of R exposure as of February 2002. This is half the final exposure depth, so we

expect that this initial sample will not go as far down the mass function (and perhaps not as far in redshift) as the final sample.

The individual exposures of a given area of sky were coadded, and the resulting deep images were cataloged by SExtractor.[24] These catalogs were then input to the *ellipto* algorithm,[25] which derives weighted second central moments for each object cataloged by SExtractor. This weighting scheme is mathematically equivalent to finding the best-fit elliptical Gaussian shape of each source.

Many of the subfields were adjacent to other qualifying subfields, so we combined these catalogs into supercatalogs, one for each distinct field. This provides a great advantage in minimizing edge effects. Near the edge of a catalog area, a mass map becomes noisier because of the lack of constraining data. With constraining data provided by an adjacent subfield, the increase in noise is avoided. The perimeter of the supercatalog is *much* shorter than the sum of the perimeters of the individual catalogs, so the loss of area to increased noise is greatly reduced.

In stitching together these catalogs, care must be taken to insure that the astrometry, photometry, and morphology of objects in the overlap area are well matched. We rejected objects in the overlap area which did not meet any of several quality checks: the various aperture magnitude measurements must differ less than 0.2 magnitudes, and all the second central moments must differ by less than 1 pixel squared. The rejection rate was low (less than 20% in all cases). The validity of the astrometry was confirmed by the paucity of sources in the overlap region whose position did not match any source from the adjacent subfield.

These supercatalogs were then winnowed of sources which were likely to be spurious, to lack well-measured shapes, or to be at low redshift. Sources meeting any of the following criteria were rejected:

- SExtractor flags > 4. This includes saturated sources (which are stars), sources too close to the edge to properly measure, and other fatal errors. Acceptable warning flags include proximity to another source, because we let ellipto determine if proximity is a problem.
- nonzero *ellipto* errorcode. Errorcodes can be triggered by various conditions, the most common being that the centroid of the source as determined by *ellipto* does not match the SExtractor position, which usually indicates that the source is very near or blended with another source.
- measured ellipticity > 0.5. Our simulations of the Hubble Deep Field and synthetic

fields convolved with typical DLS point-spread function ($\sim 0.9''$ FWHM) indicate that the vast majority of sources with measured ellipticity > 0.5 are actually blends of two different sources. This cut eliminates about 15% of the sources.

- size at least 25% larger than the PSF size (must be well resolved to measure shape accurately)
- R magnitude between 23 and 25, and isophotal area less than 150 pixels (10 arcsec^2). These criteria eliminate low-redshift galaxies which are unlikely to be lensed due to lack of intervening structures.

In each field, this filtered sample was used to make a convergence map. Convergence maps are often colloquially called mass maps. The distinction between convergence and mass has already been explained, but this distinction is not important here as we are looking for variations in density rather than yield truly calibrated masses. Convergence maps are produced by convolving the shear field (as measured by galaxy ellipticities) with a lensing kernel which is smoothed somewhat to avoid divergent noise on small scales; see Ref. 26 for a clear introduction to the algorithms of lensing. We used the kernel of Fischer & Tyson.[27]

3.2 Mass maps

Figures 4 through 7 present the "mass" (convergence) maps for DLS fields F2 through F5 (see Table 1 for coordinates of field centers). In all figures, north is up and east is to the left. At the time these maps were constructed, fields F3 and F5 had not been imaged over their full area. Images are taken in blocks of 40' square (the size of the Mosaic field of view), which are called subfields. The F2 and F4 mass maps have a full 3×3 array of subfields making a complete $2^\circ \times 2^\circ$ area. The F3 mass map covers four contiguous subfields in an "L" shape, and the F5 mass map covers just two adjacent subfields. This makes a total of 24 subfields, or 10 deg^2. In this section we comment on each field; comments on individual clusters appear in the next section.

First, a general observation: In many cases, the mass maps show peaks which do not correspond to already-known clusters (as listed in NED, the NASA/IPAC Extragalactic Database, `http://nedwww.ipac.caltech.edu`). Conversely, many of the clusters listed in NED are not detected in their shear signal. (On average, NED lists about five clusters per 2-degree field.) This is not surprising, given the different redshift sensitivities of the techniques involved. For lensing with background sources at

Field	RA	DEC	l,b	E(B-V)
F1	00:53:25.3	+12:33:55	125,-50	0.06
F2	09:18:00	+30:00:00	197, 44	0.02
F3	05:20:00	-49:00:00	255,-35	0.02
F4	10:52:00	-05:00:00	257,47	0.025
F5	13:55:00	-10:00:00	328,49	0.05

Table 1. Field information. Coordinates are J2000, at the field center. Extinctions are from the maps of Schlegel *et al.*[28] and represent rough averages over large areas which vary somewhat.

a redshift of 1–2, sensitivity to mass concentrations has a broad peak at $z \sim 0.5$, falling to zero at $z = 0$, whereas for existing optical and X-ray surveys, sensitivity falls off as the square of the luminosity distance. Furthermore, on a random area of sky, known clusters are likely to be from shallow all-sky surveys, not covered by more modern, deeper but smaller-area surveys. For that reason, a real comparison of optical and shear selection must employ optical selection on the deep DLS imaging itself, and that work is in progress.

3.2.1 F2

The mass map for this field covers a full $2^\circ \times 2^\circ$ area (Figure 4). The most prominent mass concentration, DLS Cluster 1, has three distinct subclumps in both mass and X-ray maps (see below).

3.2.2 F3

Figure 5 shows a convergence map covering four subfields. The two most prominent mass peaks correspond to already-known clusters; this happens to be a region rich with already-known clusters. The second most prominent mass peak, in the bottom right corner of the active area, did not make it into the sample because it was too close to the edge of the data to be considered reliable (see below for edge criteria). However, when the full area of F3 is completed, this cluster will no longer be on the edge, and will make it into the final sample.

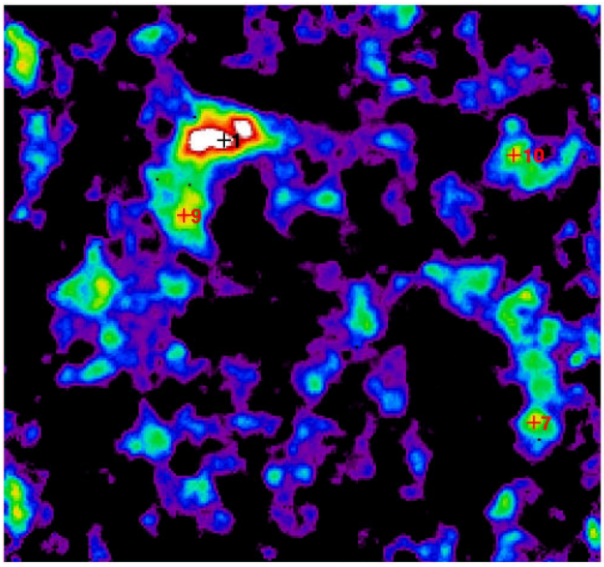

Fig. 4. Mass map for field F2, covering a full $2^\circ \times 2^\circ$ area. In all maps, black indicates low surface mass density, white indicates highest density; north is up, east is left; and labels indicate DLS cluster number.

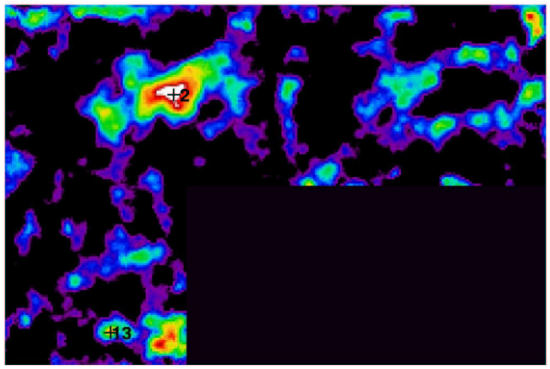

Fig. 5. Mass map for part of field F3, covering 45% of the final area.

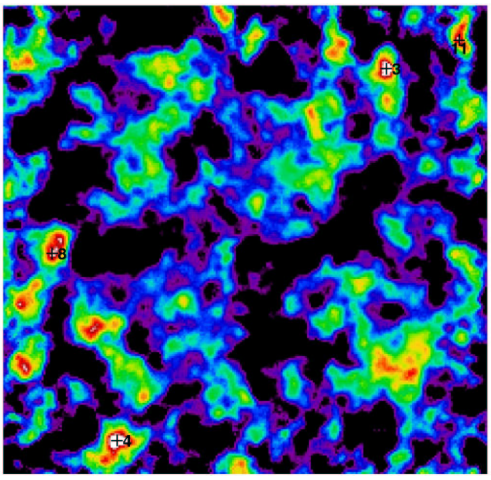

Fig. 6. Mass map for field F4, covering the full $2^\circ \times 2^\circ$ area.

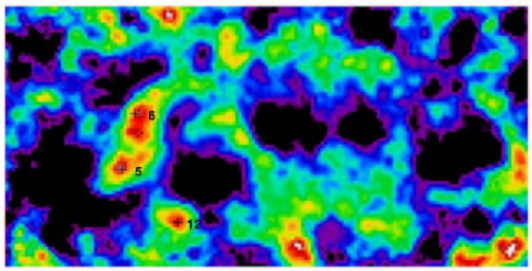

Fig. 7. Mass map for part of field F5, covering 22% of the final area.

3.2.3 F4

All nine subfields are shown in Figure 6. Cluster 8 at center left has been spectroscopically confirmed at $z = 0.68$ and is detailed elsewhere.[8] None of the prominent mass peaks correspond to already-known clusters. In fact, this is a region which happens to be quite deficient in already-known clusters.

3.2.4 F5

Only two subfields are shown in Figure 7. NED lists no clusters in this region, which is hardly surprising given the small amount of area.

3.3 Cluster Candidates

For each field, we also made maps of the gravitational potential, which simply involves modifying the radial dependence of the convolution kernel. Although the information in the two maps is not independent, the noise properties are somewhat different, so if the peaks in the mass maps had significant contributions from noise, we would expect them to disappear or be greatly reduced in the potential maps. Thus the potential maps provided a very limited form of confirmation in the absence of photometric redshifts derived from imaging at other wavelengths. The potential maps are not presented here because they present the same large peaks as do the convergence maps. The differences are only at levels well below the clusters marked here.

Note that we have not calibrated the source redshift distribution given the source selection criteria above. Therefore we seek not an absolute measure of surface density, but a relative ranking of the peaks in arbitarary units. These peaks will then be followed up with more extensive analysis using both DLS and non-DLS data. The DLS data will provide photometric redshifts of cluster members should cluster members be obvious, and a rough lens redshift from weak lensing tomography[7,8] if not. Note that photometric redshifts require full $BVRz'$ imaging, so many of the clusters detected here have not yet been followed up with such an analysis. Followup with complementary instruments includes spectroscopy of cluster members and X-ray spectro-imaging with Chandra and XMM.

We compiled a list of peaks and then eliminated those within 5' of an edge. This incurs a loss of effective area, but insures against the increase of noise at the edge. Some of the edges are only temporary, to be extended with more imaging, so we expect some of the eliminated candidates to return when the full dataset is reprocessed uniformly.

We then ranked peaks according to their heights in the convergence and potential maps. The two lists agreed closely near their tops and much less closely near their bottoms. This gave us some indication of the noise level, and we cut the list where we were confident that all candidates above the cut were real, yielding 16 candidates. Of these, the top eight have been observed with Chandra; the next three are scheduled for XMM time, and the next two are conditionally scheduled for XMM time, for a total of 13 clusters with X-ray followup. The final list of clusters will appear in a future paper when the analysis is more complete. Here, we present a sampling of mass and X-ray maps, and comments on redshifts and optical morphologies, to demonstrate the variety of the sample.

3.4 Details of Cluster Candidates

In this section we present details on each cluster candidate, where available. Some of the X-ray followup data has yet to be acquired, and other data have arrived so recently that analysis is just beginning. We therefore present some X-ray maps to give an impression of the relation between mass and X-rays, but reserve a real analysis for a forthcoming paper.

The X-ray maps presented below were taken by the ACIS instrument aboard Chandra. ACIS has a field of view of $16'$ and a resolution of about $1''$. Point sources have been removed so that extended sources are more obvious (all clusters will be extended, whereas point sources will generally be active galactic nuclei, in galaxies which may not be associated with the cluster). The underlying data contain spectral information which is not visible here. Derivation of temperatures from the X-ray data is in progress. To complement the X-ray maps, we present convergence maps of the same area, but with lower resolution, limited by the source statistics to about $1'$.

3.4.1 DLS Cluster 1

This is the most prominent mass concentration in F2, and the optical imaging shows a rich cluster. The redshift is well-known at 0.298. Chandra X-ray spectro-imaging shows three distinct subclumps, just as the massmap does. The two maps agree on the gross details such as the number and location of subclumps, but the differences in emphasis suggest a more complex relationship between mass and X-ray emission. A detailed paper on this cluster is in preparation. Our preliminary estimate of the X-ray luminosity is 8.5×10^{44} erg s^{-1}.

3.4.2 DLS Cluster 2

This is the most prominent mass concentration in the 40% of F3 which has been mapped. The X-ray map shows two clearly extended sources (Figure 8). One is located $2'$ from the mass peak, and the other is $5'$ from the mass peak. This second X-ray source does not appear clearly on the convergence map, although it may be a contributor to what is a very broad feature in the convergence map. Two additional X-ray sources are weaker and may be due to single galaxies.

We have applied for spectroscopy to determine the redshift of this cluster, and to explore whether it is in fact several clusters.

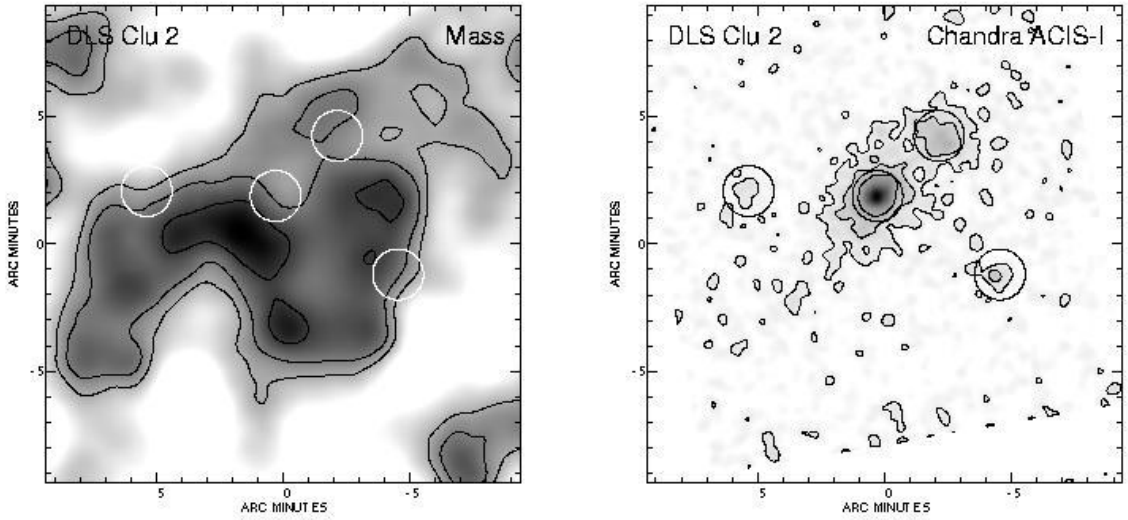

Fig. 8. DLS Cluster 2. Left: convergence. Right: X-ray. The field size is $16'$ on a side. Circles indicate positions of X-ray sources.

3.4.3 DLS Cluster 3

This mass concentration dominates the northwestern part of field F4. There is X-ray emission within $1'$ of the mass peak. (Recall that the resolution of the convergence maps is $\sim 1'$.) However, this X-ray emission is not clearly extended. Its position is centered right on a very bright galaxy, which may have an active nucleus giving rise to the X-ray emission. On the other hand, the optical imaging clearly shows a cluster of galaxies surrounding this galaxy. We are currently working to understand what fraction of the X-ray emission comes from the hot intracluster medium (which follows the cluster's gravitational protential) and what fraction comes from the galactic nucleus (which should be ignored when studying the cluster as a whole).

This cluster has not been previously identified, and none of its members have redshifts listed in NED. We have applied for spectroscopy to determine the redshift of this cluster.

3.4.4 DLS Cluster 4

This cluster is located at the southern end of F4. The optical imaging clearly shows a cluster of galaxies. Although this is not listed as a cluster in NED, NED does list 5–10 galaxies in the area at z=0.18-0.19. Therefore we have not applied for spectroscopy; $z = 0.18$ is a working hypothesis until the photometric redshift analysis either confirms it or demands additional spectroscopy.

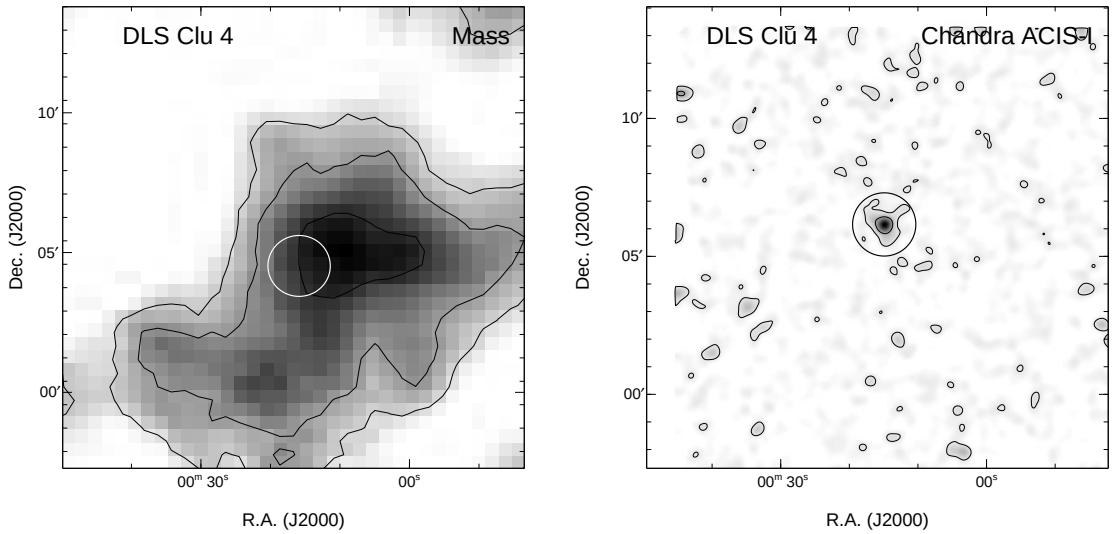

Fig. 9. DLS Cluster 4. Left: convergence. Right: X-ray. The field size is 16′ on a side.

Figure 9 shows the convergence and X-ray maps. There is an X-ray source within 2′ of the mass peak and coincident with a bright galaxy. The emission is extended, but not greatly. At $z = 0.18$, the X-ray luminosity is low for a cluster, 4.3$\times$ 10^{42} ergs s^{-1}.

3.4.5 DLS Cluster 5

This is the more southern of the two candidates in F5. The optical imaging shows a cluster of red galaxies which appears to be at fairly high redshift, given their small angular size. The location of the cluster center is difficult to define, but the peak on the mass map is less than 30″ from any plausible center. Another group apparently at lower redshift (i.e. with larger and less red galaxies) appears 2.5′ to the east. However, the lensing signal has dropped to quite a low value at that point, so we are confident in our identification.

There is no extended X-ray emission, and there are no known clusters or galaxies with known redshifts within 5′ of this location. Spectroscopy of the cluster and nearby group is planned.

3.4.6 DLS Cluster 6

This mass concentration lies only 9′ north of the previous cluster. Again, there is no extended X-ray emission, and there are no known clusters or galaxies with known

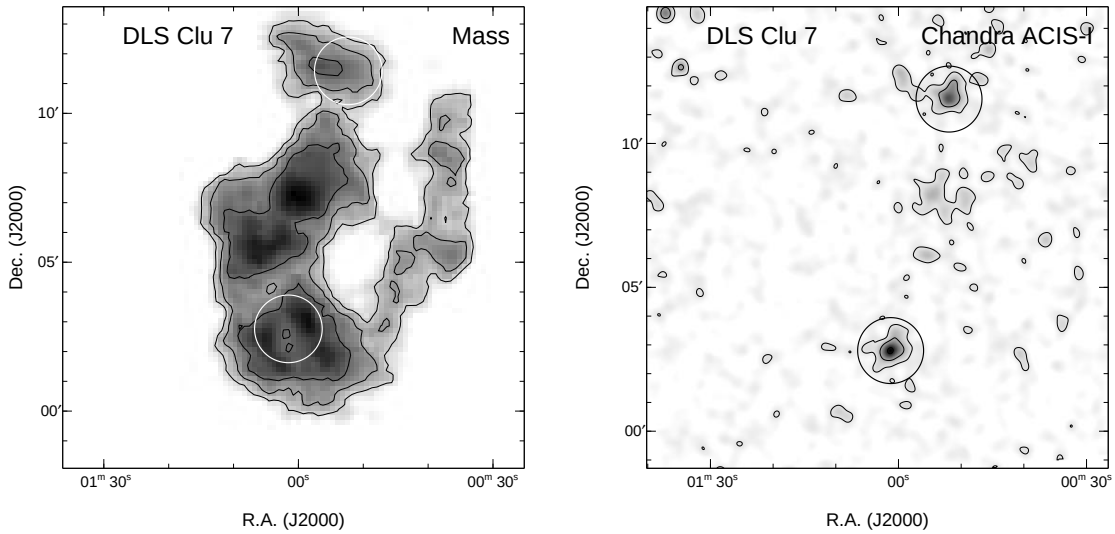

Fig. 10. DLS Cluster 7. Left: convergence. Right: X-ray. The field size is $16'$ on a side.

redshifts within $5'$ of this location. In this case, there is not even a clear concentration of galaxies in the $BVRz'$ imaging. However, there is a secondary peak on the mass map $3'$ to the south, and this corresponds to a large concentration of galaxies. A thorough analysis with photometric redshifts may be able to determine whether the two mass concentrations are at the same redshift.

3.4.7 DLS Cluster 7

This mass concentration appears in the southwest of F2. It does not stand out in the F2 convergence map (Figure 4) because it lies on a north-south ridge. In fact there is a filamentary concentration of red galaxies at this location, but it may well be a superposition of unrelated groups of galaxies.

Figure 10 shows the convergence and X-ray maps. The X-ray data show two extended sources bracketing the location of the mass peak along the string of galaxies. One of them is coincident with a definite cluster of small red galaxies, directly behind three very bright ($\sim 12^m$) stars. Because of the bright stars, one might easily overlook this cluster when perusing the images, but the X-ray and lensing techniques are unperturbed by the bright stars—X-ray because most stars do not emit much X-ray radiation, and lensing because a lens makes its shear felt even at a large impact parameter. At the location of the other X-ray source, there is a more diffuse grouping of small red galaxies. Note that

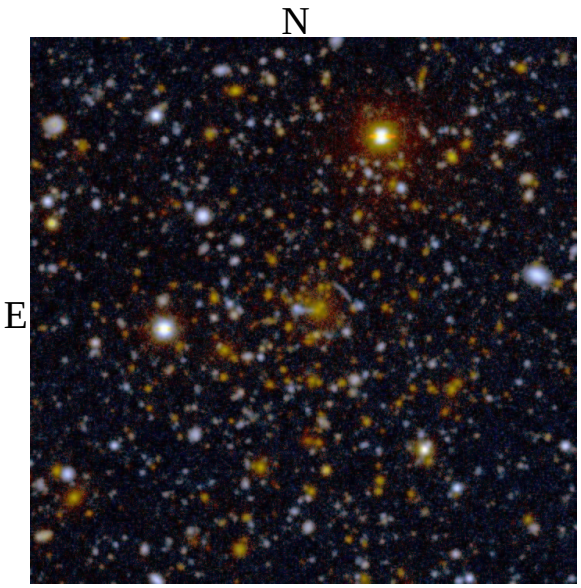

Fig. 11. DLS Cluster 8 at $z = 0.68$. The image is a BVR composite, $3'$ on a side. The tangential arc is $10''$ northwest of the brightest cluster galaxy.

the linear-appearing concentration of galaxies extends only 10–$15'$, only one-third the extent of the feature in the mass map. Much of the ridge in the mass map is at a low level and of unclear significance.

The literature contains no cluster or galaxy of known redshift within $5'$. We have applied for followup spectroscopy.

3.4.8 DLS Cluster 8

This cluster appears at center left in the F4 mass map. It is detailed elsewhere,[8] but a brief description is in order here. The $BVRz'$ imaging shows a beautiful concentration of small red galaxies (Figure 11), with what appear to be strong lensing features: A large blue tangential arc, and an opposing blue radial arc. This was the first cluster for which we organized followup, because it was so clearly interesting. Keck spectroscopy showed it to be at $z = 0.68$ with a velocity dispersion of 980 km s^{-1}. A tomographic weak lensing analysis with photometric redshifts yielded a similar redshift and a mass estimate of $11.1 \pm 2.8 \times 10^{14}\ (r/Mpc)\ M_\odot$ within radius r, using a singular isothermal sphere profile. This mass is in agreement with the velocity dispersion and strong lensing constraints.

Figure 12 shows the convergence and X-ray maps. An extended X-ray source is found at the location of the cluster. Armed with a redshift, we compute a preliminary X-

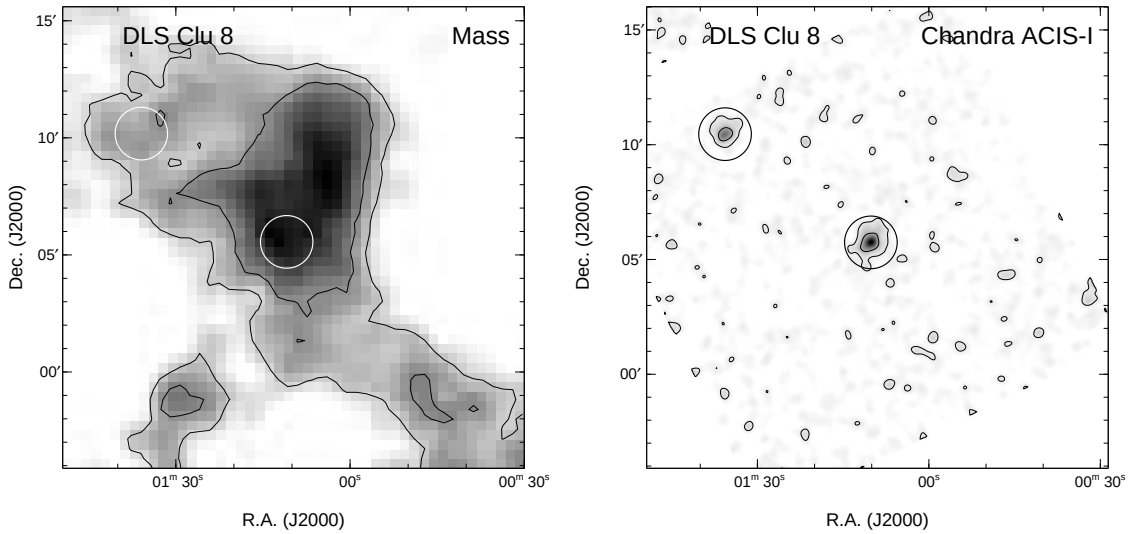

Fig. 12. DLS Cluster 7. Left: convergence. Right: X-ray. The field size is 16′ on a side.

ray luminosity of 1.7×10^{44} erg s^{-1}. A second X-ray source to the northeast corresponds to a slight bump in the convergence map. The redshift of this object is unknown.

3.4.9 DLS Cluster 9

This cluster lies just 16′ south (and a bit eastward) of DLS Cluster 1. Its position corresponds to a fairly rich cluster of small red galaxies. X-ray data are not available yet. The literature contains no cluster or galaxy of known redshift within 5′.

3.4.10 DLS Cluster 10

DLS Cluster 10 lies in the northwest quadrant of F2. Its position is puzzling: There are no galaxies in the immediate area, but there is a cluster of galaxies 3′ to the northwest. This displacement is much larger than the resolution of the mass maps. The literature contains no cluster or galaxy of known redshift within 5′ of either position. X-ray data are not available yet. Analysis with photometric redshifts will reveal whether the cluster and the lens are at the same redshift, and perhaps explain why the cluster does not appear clearly on the convergence map.

3.4.11 DLS Cluster 11

This mass peak appears in the extreme northwest corner of F4. Its position is on the edge of a group of large (i.e. low-redshift) galaxies. There are a few 2dFGRS[29] galaxies with known redshift in the area, but not enough to come to any conclusions about the redshift of the group. Analysis with photometric redshifts is needed to conclusively identify the lensing mass with the group. X-ray data are not available yet.

3.4.12 DLS Cluster 12

This cluster is in F5, southwest of the more significant DLS Clusters 5 and 6. This is another puzzling mass concentration: It is $6'$ west of an obvious cluster of galaxies, which does not appear on the mass map. There is a compact group of small, red galaxies $2'$ to the northeast, but it is not clear that we can identify this group with the lens. The literature does not contain a cluster at either position, nor any useful galaxy redshifts. Again, more analysis is required. Unfortunately, we may not get X-ray data on this candidate and the next one: They are in a group of XMM targets which will be observed only if time permits.

3.4.13 DLS Cluster 13

This mass concentration lies at the southern end of the analyzed portion of F3. A more impressive-looking peak appears just $10'$ west of DLS Cluster 12 in Figure 5, but that peak was too close to the edge to appear in the current sample. (Those edges will be filled in by ongoing imaging.) This is the mass concentration about which we know the least: There is no obvious clustering of galaxies in the vicinity, no X-ray data yet, and no relevant information in the literature.

3.5 General Remarks and Ongoing Analysis

High rank on the mass concentration list clearly correlates with ease of identification with clusters of galaxies (already-known clusters in the case of the top two), and detection of extended X-ray sources. Our sample may have a generally high mass-to-light ratio (M/L) compared to optically and X-ray selected clusters, with only the most massive clusters generating enough light to be detected by other means. On the other hand, the low-ranked mass concentrations may be more affected by noise and/or edge effects than we estimated when compiling the list.

Fortunately, we can answer this question by analyzing the complete set of DLS data. Once the full $BVRz'$ imaging in a given area has been cataloged, photometric redshifts will provide definitive proof of the reality of the lower-ranked clusters. If some error in a mass map has resulted in a spurious peak which is apparently significant, the strength of that peak should not correlate with source redshift. If there is the expected trend with source redshift, that provides not only confirmation but also a rough lens redshift. In addition, by adding in the missing areas in some fields, we will greatly reduce any edge effects which might be present in the current geometry.

Clearly, the first task is to obtain redshifts for each of our mass concentrations and related clusters of galaxies. Photometric redshifts built into the DLS will solve most of the puzzles presented above, but in many cases we are still planning on spectroscopy. This is because we want a rock-solid redshift to go with each X-ray detection. Photometric redshift systematics are currently at the 5–10% level. Although we believe we can improve that, the X-ray luminosity still depends on the square of this quantity. Therefore we need spectroscopic redshifts for accurate X-ray luminosities and optical mass-to-light ratios.

Armed with redshifts, we will then derive $M - L_X$ (mass–X-ray luminosity) and $M - T_X$ (mass–X-ray temperature) relations for our sample, to be compared with the same relations for X-ray selected samples. We will also derive optical M/L ratios for the clusters, to be compared with typical M/L for optically-selected samples. At the same time, we will search our data using optical selection techniques, and produce a DLS optically-selected cluster sample. The overlap between this sample and the shear-selected sample will be especially interesting, because we can compare on a cluster-by-cluster basis.

Finally, much work remains to be done on refining the lensing selection. Once photometric redshifts are available, should we integrate them into the search rather than use them as followup? What filters and convolution kernels are optimal? With an optimal search technique, can we go further down the list and derive a larger sample? This is important work, but it should not obscure the fact that we already have a small, uniformly selected sample of significant detections.

4 Summary

The DLS is a deep optical imaging survey which combines photometric redshifts with weak gravitational lensing to probe the mass distribution in the universe in three dimen-

sions (or equivalently, as a function of cosmic time). Most of the data have already been taken, data processing is ongoing, and early results show that this three-dimensional probe will be effective. The main result presented here is the first-ever sample of shear-selected clusters, from R-band imaging over ~ 10 deg^2. This sample will be extended by deeper imaging, a factor of two more area, and the addition of color (hence photometric redshift) information. Nevertheless, with the smaller initial sample we are already beginning to investigate potential differences between shear-selected samples and more traditional optically and X-ray selected samples. The motivation here is that while traditional samples are much more extensive and mature, they may underrepresent low-luminosity clusters. To that end, we are currently analyzing X-ray data from Chandra and XMM with the goal of deriving $M - L_X$ and $M - T_X$ relations for our sample. These relations will then be compared with the same relations for X-ray selected samples.

References

[1] Spergel, D. N. et al. 2003, *ApJ Suppl.*, 148, 175

[2] Schneider, P. 1996, *Monthly Notices of the Royal Astronomical Society*, 283, 837

[3] Abell, G. O., Corwin, H. G., & Olowin, R. P. 1989, *ApJ Suppl.*, 70, 1

[4] Gladders, M. D. & Yee, H. K. C. 2000, *Astronomical Journal*, 120, 2148

[5] Borgani, S. & Guzzo, L. 2001, *Nature*, 409, 39

[6] Carlstrom, J.E., Holder, G.P. & Reese, E.D., 2002, *ARAA*, 40, 643

[7] Wittman, D., Tyson, J. A., Margoniner, V. E., Cohen, J. G. & Dell'Antonio, I., 2001, *ApJL* 557, L89

[8] Wittman, D., Margoniner, V. E., Tyson, J. A., Cohen, J. G. & Dell'Antonio, I. & Becker, A. C., 2003, *ApJ*597, 218

[9] Dahle, H., Pedersen, K., Lilje, P. B., Maddox, S. J., & Kaiser, N. 2003, *ApJ*, 591, 662

[10] Schirmer, M., Erben, T., Schneider, P., Pietrzynski, G., Gieren, W., Micol, A. & Pierfederici, F., 2003, *A&A*, submitted, astro-ph/0305172

[11] Erben, T., van Waerbeke, L., Mellier, Y., Schneider, P., Cuillandre, J.-C., Castander, F.J. & Dantel-Fort, M. 2000, A&A 355, 23

[12] Umetsu, K. & Futamase, T. 2000, *ApJL* 539, L5

[13] Clowe, D., Trentham, N., & Tonry, J. 2001, *A&A*, 369, 16

[14] J.-M. Miralles *et al.* 2002, *A&A*, 388, 68

[15] Weinberg, N. N. & Kamionkowski, M. 2002, *Monthly Notices of the Royal Astronomical Society*, 337, 1269

[16] Wittman, D. *et al.*, *Proc. SPIE*, 4836, 73 (2002)

[17] Kent, S., 2003, these proceedings

[18] Fischer, P. et al. 2000, *Astronomical Journal*, 120, 1198

[19] Sheldon, E. S. et al. 2001, *ApJ*, 554, 881

[20] Jannuzi, B. T., Dey, A., Brown, M. J. I., Tiede, G. P., & NDWFS Team 2002, *Bulletin of the American Astronomical Society*, 34, 1271

[21] Le Fevre, O. et al. 2003, *Proc. SPIE*, 4834, 173

[22] Shimasaku, K. et al. 2003, *ApJL*, 586, L111

[23] `http://www.cfht.hawaii.edu/Science/CFHLS/`

[24] Bertin, E. and Arnouts, S. 1996, *A&A Supp.* 117, 393

[25] Bernstein, G. M. & Jarvis, M. 2002, *Astronomical Journal* 123, 583

[26] Narayan, R. & Bartelmann, M. 1999, Formation of Structure in the Universe, 360 (astro-ph/9606001)

[27] Fischer, P. & Tyson, J. A. 1997, *Astronomical Journal* 114, 14

[28] Schlegel, D. J., Finkbeiner, D. P., & Davis, M. 1998, *ApJ*, 500, 525

[29] Colless, M. et al. 2003, VizieR Online Data Catalog, 7226